Itinerant ferromagnetism in a spin-fermion model for diluted spin systems

Sourav Chakraborty, Sandip Halder, and Kalpataru Pradhan[*]

Theory Division, Saha Institute of Nuclear Physics, A CI of Homi Bhabha National Institute, Kolkata-700064, India

We investigate itinerant ferromagnetism using a diluted spin-fermion model, derived from a repulsive Hubbard model, where itinerant fermions are coupled antiferromagnetically to spin auxiliary fields in a three-dimensional simple cubic lattice. We assign a positive finite value ($\sim$bandwidth) to the Hubbard on-site potential (U) at a fraction of sites to model magnetic impurities and set $U = 0$ for rest of the sites, which corresponds to the nonmagnetic sites. In this inhomogeneous Hubbard-model representation for randomly distributed magnetic impurities, which is an appropriate model to study diluted spin systems like diluted magnetic semiconductors, itinerant carriers are confined to the impurity band and play a key role in determining the kinetic energy of the system and, consequently, the carrier-spin polarization. We focus, in particular, on understanding the spin-dependent transport properties of itinerant fermions in the impurity band by taking positional disorder of the auxiliary fields into account. Our semiclassical Monte Carlo calculations show that the ferromagnetic transition temperature of the carrier spins indeed shows an optimization behavior with the carrier density, similar to experimental observation in diluted magnetic semiconductors. We calculate the transport properties in detail to establish a one-to-one correspondence between the magnetic and transport properties of the carriers. In addition, the spin-polarized resistivities and density of states show that the system turns out to be a half-metallic ferromagnet. Overall, our results obtained beyond the perturbative regime are significant for understanding the ferromagnetism in diluted magnetic semiconductors.

I. INTRODUCTION

The history of magnetism is very old but scientists have begun to understand the concept during the 20th century [1]. A detailed understanding of magnetism is always necessary to invent and design unique magnetic materials [2–5]. As of now, microscopic description of itinerant ferromagnetism still remains a subject of intense research [6–10]. Due to the technological applications, even today the study of itinerant ferromagnetism remains one of the most interesting as well as challenging avenues for both experimental and theoretical condensed matter physicists.

In recent years, significant progress has been made in understanding magnetic ordering using the microscopic theories of itinerant magnetism. In 1938, the Stoner model was first introduced to interpret itinerant ferromagnetism [11]. In his phenomenal work, Stoner pointed out that ferromagnetic (FM) order can arise due to the interaction among the itinerant electrons, which spin spilt the electronic band structure. For various metals, such as Fe, Co, and Ni, the itinerant electrons exhibit FM behavior [11,12]. In these materials, electrons whose spins align to form a FM state are extended and give rise to metallicity. This itinerant carrier-driven ferromagnetism also appears in $3d$ and $4d$ electron systems like, $ZrZn_2$ [13], doped-manganites [14], doped-cobaltites [15], and strontium ruthenate [16].

Prior to Stoner, one of the first justifications of quantum ferromagnetism was put forward by Heisenberg, who established that the exchange interactions, arising due to spin-dependent Coulomb repulsion, drives the magnetism between localized moments [17]. The Heisenberg model both in classical and quantum forms remains one of the finest and oldest tools to explain the magnetism and related physical observables in strongly correlated magnetic insulators [18–21]. Although a FM Heisenberg model is explored to understand itinerant ferromagnetism [22], the real difficulty lies in arriving at the effective Hamiltonian of an interacting spin system with negative exchange coupling [20]. Ferromagnetic kinetic exchange between localized spins that arises from an interplay of spin and orbital degrees of freedom is relatively rare [23].

However, probing ferromagnetism in diluted FM semiconductors using the Heisenberg model is limited [24–26]. Dual semiconducting and magnetic properties of FM semiconductors [27,28], a diluted spin system, where magnetic impurities are doped in a host semiconductor, is expected to bring technological revolution in spintronics [29–31]. Theoretical investigation is necessary to understand the physics of these materials that will help us to push the FM transition T_C beyond room temperature [32].

In this class of diluted spin systems, the magnetic impurities provide both itinerant carriers and localized moments [31,32]. The itinerant carriers reside in the shallow acceptor level introduced by magnetic impurity ions in the host semiconductor band gap. It is widely accepted that the (exchange) interaction between the magnetic spins is mediated by the itinerant electrons [33–37]. This warrants an additional

interband coupling between the itinerant carriers and the localized moments to study the magnetic and transport properties of charge carriers.

To understand the physics of spin splitting in the carrier impurity band (IB) from the perspective of an *itinerant-exchange* mechanism, we focus on the strong coupling limit. In this limit, carriers are firmly localized to the impurity sites and, as a result, the acceptor levels give rise to a distinct IB [38,39]. Although the IB picture in the most studied GaMnAs semiconductor remains controversial to date [40–43], the addition of Mn to GaN like large band-gap semiconductors give rise to a deep IB within the host band gap [44–46]. Moreover, a crossover between the valence band to IB picture was obtained in GaMnAs with reduction in Mn doping [47]. In addition, a resonant tunneling spectroscopy investigation concluded that the Fermi level is not located below the valence band maxima in GaMnAs [48]. Besides, positive magnetic circular dichroism background signal caused by the optical transitions indicates the presence of an IB in the band gap [49]. Observation of high effective mass of the holes and a red-shifting of the midinfrared resonance of optical conductivity also suggest that the carriers are residing within the IB [50]. Another important identification of the IB is the optimization of FM T_C with respect to effective carrier density as the carriers at the band edges of the IB are more localized than at midband region [43]. However, it remains debated whether the carriers in GaMnAs reside in the valence band or in an IB [31,32,51].

Due to disorder (antisite disorder [52] and interstitial defects [53]), the IB remains less than half filled, i.e., carrier density remains smaller than the impurity density and the Fermi energy lies in the IB. The position of the Fermi energy, decided by the density of the itinerant carriers, plays a key role in determining the kinetic energy of the system. Consequently, the gain in kinetic energy is considered a major factor that decides the carrier-spin polarization. Surprisingly, to the best of our knowledge only one study so far has been carried out by implementing the Hubbard-model representation of randomly distributed magnetic impurities to study carrier-mediated FM ordering in diluted magnetic semiconductors [54]. The microscopic correlated lattice fermion model implemented in Ref. [54] treats the impurity concentration, impurity disorder, and electron correlation on equal footing. In that work, the collective magnetic response in the FM state was carried out within a mean-field-plus-spin-fluctuation approach. Further, detailed studies comprising carrier-spin-dependent transport of localized carriers are limited to date.

In this paper, we focus on the spin-dependent transport properties of the carriers confined to the IB. In our effective spin-fermion model Hamiltonian, derived from repulsive Hubbard model, we assign the $U \sim BW$ (bandwidth) on a small percentage of sites in a simple cubic lattice and set it to zero for the rest of the sites. We take the carrier density with respect to the impurity concentration, which is concomitant with experimental measurements. We organize this paper as follows: In Sec. II, we introduce the effective spin-fermion model derived from the Hubbard Hamiltonian and outline our method. We frame the IB scenario in Sec. III. In Sec. IV, we present our numerical results, comprising spin-dependent transport of carriers for $U \sim BW$. Section V is dedicated to compare the magnetic and transport properties by varying the

on-site interaction U. Section VI is devoted to analyzing our main results for two different concentration of the impurities. Finally, in Sec, VII we summarize our results.

II. MODEL HAMILTONIAN AND METHOD

We consider one band electron-hole symmetric Hubbard Hamiltonian

$$H = -t \sum_{<i,j>,\sigma} (c_{i,\sigma}^\dagger c_{j,\sigma} + \text{H.c.})$$
$$+ U \sum_i \left(n_{i,\uparrow} - \frac{1}{2}\right)\left(n_{i,\downarrow} - \frac{1}{2}\right),$$

where the first term is the kinetic energy [t is the nearest-neighbor hopping parameter and $c_{i\sigma}^\dagger$ ($c_{i\sigma}$) are the fermion creation (annihilation) operators at site i with spin σ] and the second term represents the repulsive Hubbard interaction ($U > 0$).

We reduce the quartic fermion problem present in the repulsive Hubbard model into a quadratic one by introducing the Hubbard-Stratonovich field and extract the following effective spin-fermion-type Hamiltonian by suppressing the imaginary-time dependence from the Hubbard-Stratonovich fields (for details, please see Refs. [55,56]). Then, the above Hamiltonian transfers to

$$H_{sf} = -t \sum_{<i,j>,\sigma} (c_{i\sigma}^\dagger c_{j\sigma} + \text{H.c.})$$
$$+ U/2 \sum_i (<n_i> n_i - \mathbf{m}_i.\sigma_i)$$
$$+ (U/4) \sum_i \left(\mathbf{m}_i^2 - <n_i>^2\right) - \frac{U}{2} \sum_i n_i,$$

where fermions are coupled to the classical auxiliary fields ($\mathbf{m_i}$).

The nonmonotonic U dependence of the antiferromagnetic transition temperature T_N is established for undiluted system (U at all sites, i.e., $x = 1$ limit) at half filling using a semiclassical Monte Carlo (s-MC) approach [55] that matches well with determinant quantum Monte Carlo (DQMC) results [57]. Recently, we used the s-MC approach to show that the antiferromagnetic order persists beyond the classical percolation threshold in the diluted one-band Hubbard model at absolute half filling in three dimensions [56].

For diluted spin systems, we have considered finite $U \sim BW$ at randomly chosen sites k (with concentration x) and put $U = 0$ for rest of the sites (with concentration $1 - x$). Our diluted Hamiltonian is of the form [54]

$$H_{sf} = -t \sum_{<i,j>,\sigma} (c_{i,\sigma}^\dagger c_{j,\sigma} + \text{H.c.})$$
$$+ U/2 \sum_{k \in I} (<n_k> n_k - \mathbf{m}_k.\sigma_k)$$
$$+ (U/4) \sum_{k \in I} \left(\mathbf{m}_k^2 - <n_k>^2\right) - \frac{U}{2} \sum_{k \in I} n_k - \mu \sum_i n_i,$$

where I represents the randomly chosen set of impurity sites. The overall electron density n is controlled through the

chemical potential (μ) given in the last term. μ is chosen self-consistently during the thermalization process to get the desired electron density n at each temperature. In the quantum Monte Carlo method, $\mathbf{m}_k$ variables are often used as Ising-like [58–60]. These Ising-like auxiliary fields were introduced by Hirsch through a discrete Hubbard-Stratonovich transformation [61]. So, we use Ising-like auxiliary fields in our calculations. For this case the carriers are either point towards up or down direction in strong coupling limit.

We use the s-MC method to anneal the system from high temperature, consisting of randomly oriented auxiliary fields to obtain the ground state for a fixed carrier density. First, we chose a set of random auxiliary fields $\mathbf{m}_k$ at the desired number of sites and set $\langle n_k \rangle$ to be uniform for a system size of $N = L^3 = 10^3$ and calculate the internal energy of the carriers by exact diagonalization scheme. Then we update the auxiliary field at an impurity site, say k, and recalculate the internal energy of the carrier using the new auxiliary field configuration. We employ the Metropolis algorithm to accept or reject the above update. At every tenth Monte Carlo step, using the resulting $\mathbf{m}_k$ configuration, we update $\langle n_k \rangle$ self-consistently. This new set of $\langle n_k \rangle$ is used to perform the further Monte Carlo steps. To access large system size, we adopt a Monte Carlo update technique based on the traveling cluster approximation [62,63].

For impurity concentration x, we assign finite U for $10^3 x$ sites (for a system size 10^3) randomly and set $U = 0$ for the rest of the sites. We define carrier density as the electrons (or holes) per impurity site. Direct exchange interaction between the impurity spin sites is not taken into account, which is a valid approximation in the diluted limit, by avoiding the nearest-neighbor impurity pairing. All physical quantities such as carrier magnetization and conductivity are averaged over ten different positional disorder configurations of auxiliary fields in addition to the quantum and thermal averages taken during the Monte Carlo simulations. In this paper, we consider mainly $x = 0.25$, but compare our main results between $x = 0.25$ and 0.125 in the end. All parameters such as on-site repulsion (U) and temperature (T) are scaled with hopping parameter (t). We use $U \sim BW$ and vary the carrier density with respect to x from 0 to 1.

III. IMPURITY BAND PICTURE

In the IB picture, which is relevant to FM semiconductors, carriers reside in the shallow acceptor level separated from the valence band due to the strong coupling between the impurity ions and the carriers. The width of the IB and gap between IB and valence band depend upon the coupling strength. The location of the Fermi energy inside the IB plays a vital role in determining the transport and magnetic properties of the system. The optimum T_C is expected for which Fermi energy is at the center of the band to gain maximum kinetic energy from the delocalization of the carriers and supposed to decrease towards the edge of the IB.

Using our s-MC calculations, we identify that the itinerant FM order obtained in the IB picture in the spin-fermion model is due to the following scenario of events in which one type of carrier (say, up) is more mobile than the other one (down) and drives the magnetism. A schematic figure is shown in
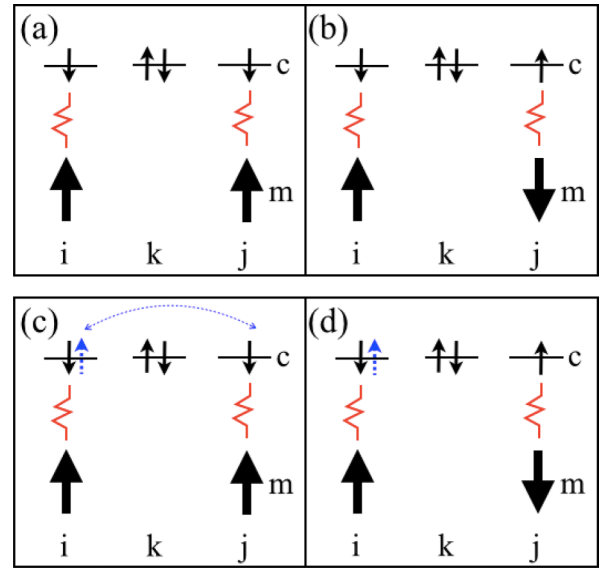

FIG. 1. Schematic: Large arrows indicate the auxiliary fields while small arrows are the carriers (shown for sites i and j). We also show the intervening nonimpurity site (k). Top Panel: Half-filling (one carrier per each impurity site) case. We find that the carriers orient randomly due to intervening nonimpurity site at half-filling. Neither (a) nor (b) are found to be the ground state. Bottom panel: Our calculations show ferromagnetic state is favored due to gain in kinetic energy via the nonimpurity site as shown in (c) when compared to the scenario drawn in (d).

Fig. 1 by assuming an IB picture where carriers are antiferromagnetically aligned to auxiliary fields at the impurity sites (sites i and j). Intervening nonimpurity site k is also shown for completeness. For the half-filling case (one carrier per each impurity site), one would naively expect an antiferromagnetic ground state mediated by carrier via the nonimpurity sites. But it is also apparent the magnetic ground state strongly depends on the magnetic impurity concentration. For $x = 0.25$, which is below the classical percolation limit ($x_p^{sc} \sim 0.31$), we do not find any magnetic ordering. This shows that the antiferromagnetic coupling between the auxiliary fields and localized carriers favors the paramagnetism at half-filling. Beyond the half-filling case, an extra electron added to the system is now relatively more mobile as the first electron is already antialigned with the auxiliary field and gives rise to the FM ground state by maximizing the kinetic energy via the nonimpurity site(s).

We start our calculation for $x = 0.25$ and use $U = 12$ ($\sim BW$) to manifest the formation of an IB that imposes the carrier localization. A well-separated IB for hole density $p = 0.2$ is clear from density of states (DOS) shown in Fig. 2(a) for a relatively high temperature ($T = 0.07$). The DOS at each ω is obtained by implementing the Lorentzian representation of the δ function: $N(\omega) = \sum_k \delta(w - w_k)$, where ω_k are the eigenvalues of the fermionic sector and the summation runs up to total number of eigenvalues ($2L^3$) of the system. The valence band is very much symmetric but the narrow IB is asymmetric. This asymmetric character of the IB picture remains intact for all the carrier densities. It is important to mention here that ferromagnetism in the Hubbard model is
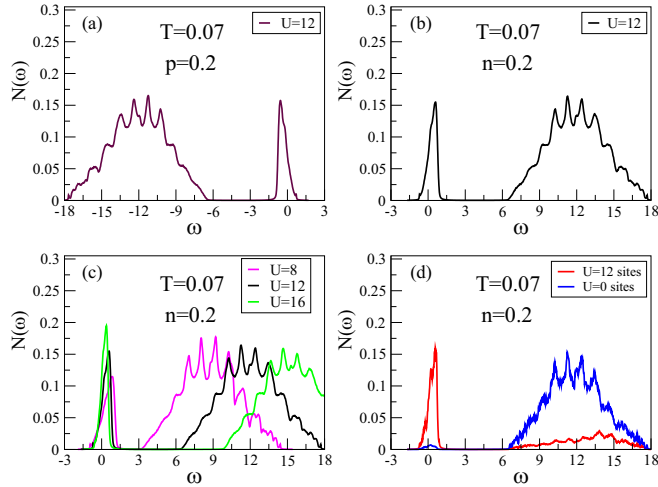
FIG. 2. Density of states for carrier density p or $n = 0.2$ at fixed $x = 0.25$ depicts a distinct impurity band for $U \sim BW$. DOS for (a) hole density $p = 0.2$ and (b) electron density $n = 0.2$ for $U = 12$. (c) The gap between the impurity band and the valence band increases with increasing the on-site interaction U and the IB shrinks. (d) Site-resolved DOS for $U = 12$ case. All the DOS are plotted for $T = 0.07$. The Fermi energy is set at zero.

attributed to an asymmetric DOS with a large spectral weight near one of the band edges [64–66].

For high band-gap systems, the ferromagnetism along with the nature of the charge carriers is still controversial. Holes (electrons) are considered to be the charge carriers for p-type conduction [31,67] (n-type conduction [68,69]) in FM semiconductors. In Fig. 2(b), we also plot the DOS using the electron density ($n = 0.2$). The structure of the IB and the position of the Fermi energy for both hole (p) and electron (n) pictures indicate that the magnetic and transport properties would provide very similar results in our s-MC calculations, which is expected from a particle-hole symmetric model Hamiltonian. So, for brevity, we performed all calculations by varying electron density n.

We plot the DOS for three different values of U in Fig. 2(c). The IB gets narrower and the gap between the valence band and IB increases with increasing U. This indicates that the carriers tend to be more and more localized in a finite region of the lattice comprised of the impurities. To substantiate this fact, we plot DOS for $U = 12$ sites and $U = 0$ sites separately in Fig. 2(d). It shows that $U = 12$ sites mostly contribute to the formation of the IB, whereas $U = 0$ sites give rise to the valence band. The contribution of $U = 12$ sites in the valence band is due to the leaking of a small amount of carriers from the impurity sites to the host lattice. This contribution decreases upon increasing the U values.

IV. SPIN-DEPENDENT TRANSPORT PROPERTIES OF CARRIERS

To analyze the carrier magnetism, first we calculate the magnetic moments M [$M = \langle (n_\uparrow - n_\downarrow)^2 \rangle = \langle n \rangle - 2\langle n_\uparrow n_\downarrow \rangle$, where the angular brackets imply quantum and thermal averaging] on each impurity ($U = 12$) site. The system-averaged quantum local moments at $U = 12$ sites for $n = 0.2$ are
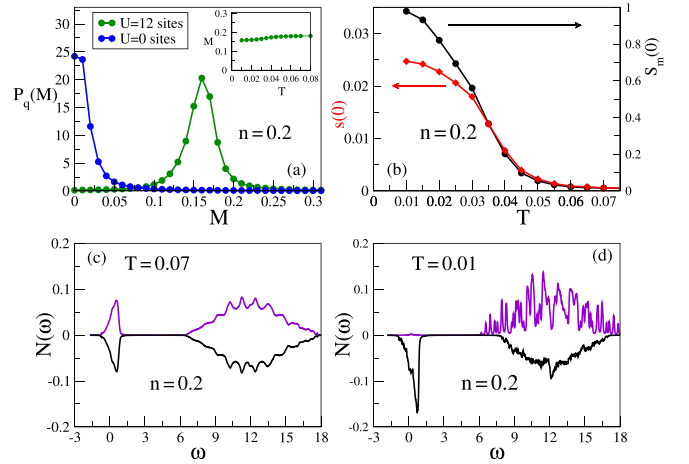

FIG. 3. Carrier spin polarization for $n = 0.2$ (using $U = 12$ and $x = 0.25$). (a) The distribution of carrier moments $P_q(M)$ for $U = 12$ (distribution for $U = 12$ sites and $U = 0$ sites are plotted separately). (b) Quantum $s(\mathbf{0})$ and classical $S_m(\mathbf{0})$ ferromagnetic structure factor versus temperature show the same transition. The spin-resolved density of states are plotted for (c) $T = 0.07$ (above T_C) and (d) $T = 0.01$ (below T_C). The equal contribution from up- or down-spin sector in (c) implies that the bands are unpolarized. For $T = 0.01$, the impurity band is completely spin polarized. The Fermi energy is set at zero.

plotted in the inset of Fig. 3(a). The average moments are approximately equal to the carrier density, barring the small change that is because of the carrier leakage to the host band as discussed in Fig. 2(d). Due to the carrier localization, for $U \sim BW$, it is expected that the formation of moments at the impurity site are more or less uniform. The local moment distribution $P_q(M) = \sum_{M_i} \delta(M - M_i)$ at $T = 0.01$ in Fig. 3(a) for $U = 12$ sites depicts this fact. The moment distribution for $U = 0$ sites, plotted separately in the same figure, shows that the moment formation in the host lattice is minimal.

Using carrier magnetic moments, we now calculate the quantum FM structure factor $s(0)$ [where $s(\mathbf{q}) = \frac{1}{(Nx)^2} \sum_{ij} \mathbf{S}_i \cdot \mathbf{S}_j e^{i\mathbf{q} \cdot (r_i - r_j)}$]. This quantum observable $\mathbf{S}_i$ (quantum spin vector) is calculated by using the eigenvectors resulting from exactly diagonalizing the equilibrated field configurations. As the quantum structure factor involves four fermionic operators, Wick's theorem is used to transform the four fermionic expectation values to combinations of two fermionic expectation values [70]. We plot the quantum FM structure factor $s(0)$ with temperature in Fig. 3(b). For $n = 0.2$, a maximum value of $s(0)$ can be 0.04 (if one gets perfect moment, i.e., $M = 0.2$ at each $U = 12$ sites). Although this is not the case here, as shown in the inset of Fig. 3(a), there is a clear FM transition.

We present the spin-resolved DOS for both high- and low-temperature cases in Figs. 3(c) and 3(d). For $T = 0.07$ (which is above T_C), the IB remains unpolarized. Both the valence band and the IB are completely symmetric for both up- or down-spin sectors. The IB is completely spin polarized for $T = 0.01$, which depicts the complete FM ordering of the carriers that reside within the IB. This agrees well with experiment [48]. In addition, we plot the classical structure factor for the auxiliary fields $S_m(0)$, where $S_m(\mathbf{q}) = \frac{1}{(Nx)^2} \sum_{ij} \mathbf{m}_i \cdot \mathbf{m}_j e^{i\mathbf{q} \cdot (r_i - r_j)}$ ($\mathbf{q}$ are the wave vectors) along with

quantum FM structure factor $s(0)$ in Fig. 3(b) and it shows the same transition. Due to strong coupling between itinerant carriers and auxiliary fields, the carriers are always aligned antiparallel to the fields. For this reason, classical FM structure factor $S_m(0)$ and quantum FM structure factor $s(0)$ behave very similar to each other.

To figure out the correspondence between the ferromagnetism and the metallicity, we analyze the temperature dependence of the resistivity for $n = 0.2$. For this, we calculate the dc limit of the optical conductivity by using the Kubo-Greenwood formula [71–73]. The procedure to calculate dc conductivity has been benchmarked in a previous work [74]. Here, we briefly outline the procedure we are currently following in this paper. The real part of conductivity

$$\sigma(\omega) = \frac{A}{N} \sum_{\alpha,\beta} \frac{n_\alpha - n_\beta}{\epsilon_\beta - \epsilon_\alpha} |\langle \psi_\alpha | j_x | \psi_\beta \rangle|^2 \frac{\Gamma}{(\omega - (\epsilon_\beta - \epsilon_\alpha))^2 + \Gamma^2}$$

[real part is defined as $\sigma(\omega)$ for brevity] that we have taken into account for our system with a finite number of energy levels is obtained from the Kubo-Greenwood formulation for the frequency-dependent electrical conductivity $\sigma_{KG}(\omega)$:

$$\sigma_{KG}(\omega) = \frac{A}{N} \sum_{\alpha,\beta} \frac{n_\alpha - n_\beta}{\epsilon_\alpha - \epsilon_\beta} \frac{-i|\langle \psi_\alpha | j_x | \psi_\beta \rangle|^2}{\epsilon_\alpha - \epsilon_\beta + i\Gamma + \omega}.$$

Here, $A = e^2/\hbar a$ (a is the lattice constant) and N is total number of lattice sites. $n_\alpha = f(\mu - \epsilon_\alpha)$ is the Fermi factor corresponding to one-electron energy level ϵ_α. $\langle \psi_\alpha | j_x | \psi_\beta \rangle$ is the matrix element of the current operator $j_x = it \sum_{i,\sigma} (c^\dagger_{i+x,\sigma} c_{i,\sigma} - \text{H.c.})$, where ψ_α, ψ_β are the single-particle eigenstates. In the limit $\Gamma \to 0$, it is known that the Lorentzian behaves like Dirac delta δ function and, as a result, the expression for $\sigma(\omega)$ becomes

$$\sigma(\omega) = \frac{A\pi}{N} \sum_{\alpha,\beta} \frac{n_\alpha - n_\beta}{\epsilon_\beta - \epsilon_\alpha} |\langle \psi_\alpha | j_x | \psi_\beta \rangle|^2 \delta[\omega - (\epsilon_\beta - \epsilon_\alpha)].$$

Then, we estimate the dc conductivity by averaging $\sigma(\omega)$ over a low-frequency interval $\Delta\omega$,

$$\sigma_{dc}(\Delta\omega) = \frac{1}{\Delta\omega} \int_0^{\Delta\omega} \sigma(\omega) d\omega,$$

where $\Delta\omega$ is taken to be four times larger than the mean finite-size gap of our finite size system (determined by the ratio of the bare bandwidth and N). At low temperature, the system shows metallic behavior as shown in Fig. 4(a). The insulator-metal transition coincides with the onset of ferromagnetism [$s(0)$ is replotted in Fig. 4(a)]. To check for the finite-size effect, which remains a concern in the small system-size-based Monte Carlo calculations, we show $s(0)$ with temperature for two system sizes $L = 10$ and 12 in Fig. 4(b). Our results indicate that the curves are pretty similar to each other.

The metallic behavior and the spin-polarized DOS [see Figs. 4(a) and 3(d)] at $T = 0.01$ indicate that the system turns out to be a half-metallic (HM) ferromagnet (HMF) at low temperature. Half-metallic systems are those for which the system shows metallicity for one spin channel and insulating behavior for the other. This behavior was first observed in Heusler alloys [75]. In fact, half-metallicity in Heusler alloys is well studied [76,77]. Recently, Co$_2$MnSi is reported
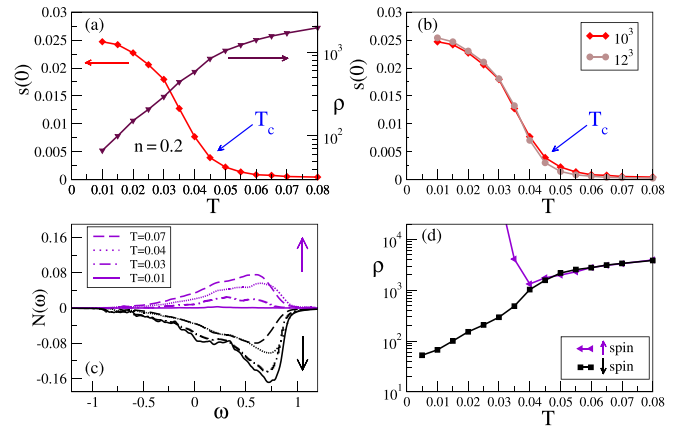

FIG. 4. Correlating ferromagnetism and metallicity for $n = 0.2$ (for $U = 12$ and $x = 0.25$). (a) Temperature dependence of resistivity in units of $\hbar a / \pi e^2$ (a is the lattice constant) shows metallicity at low temperature. Quantum structure factor $s(0)$ is also replotted here to draw a correspondence between the metallicity and the ferromagnetism. (b) Quantum ferromagnetic structure factor $s(0)$ with temperature for two system sizes using $L = 10$ and 12. (c) Spin-resolved density of states at different temperatures, where the spectral weight of the up-spin sector gradually gets transferred to the down-spin sector as temperature decreases. The Fermi energy is set at zero. (d) Temperature dependence of spin-resolved resistivities shows that system conducts through down-spin channel at low temperature.

to have spin polarization value of 93% through ultraviolet-photoemission spectroscopy [78]. Co$_2$FeAl$_{0.5}$Si$_{0.5}$ is another Heusler alloy which exhibits half-metallicity through Fermi level tuning [79]. Half-metalicity was also revealed for oxides like CrO2 [80], La$_{0.7}$Sr$_{0.3}$MnO$_3$ [81], Fe$_3$O$_4$ [82], etc. However, the accuracy of the results are scrutinized [83–86]. Reports of HM transport in high band-gap diluted magnetic semiconductors materials is limited mostly to first-principles calculations [44,87,88] where temperature effect is excluded.

Next, we verify the HMF behavior in more detail in our model Hamiltonian calculations. We present the thermal evolution of the spin-resolved IB (i.e., the DOS is plotted specifically near Fermi energy) for $n = 0.2$ in Fig. 4(c). Our calculated up- and down-DOS are pretty symmetric to each other for $T = 0.07$. The up-spin sector gradually loses the spectral weight, which gets transferred to the down-spin sector as temperature decreases. At $T = 0.01$, we find a spin-polarized system. In support, we also calculate the spin-resolved resistivity with temperature [see Fig. 4(d)]. For the paramagnetic part ($T > T_C$), the resistivity in both spin channels remain more or less equal. The resistivity for up- (down-) spin sector shows characteristics of an insulating (metallic) system at low temperatures that confirms the HM transport behavior of our system.

The moment distributions $P_q(M)$ for the different densities using only $U = 12$ sites are shown in Fig. 5(a) at $T = 0.01$. The moment distributions get steeper and the peak value [defined as $P_q(M^*)$] increases up to $n = 0.3$ and decreases thereafter. This shows that the moment distribution curve gets broadened with a reduction in $P_q(M^*)$ value on both sides
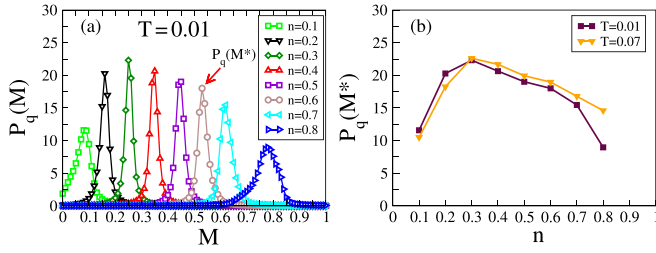
FIG. 5. Distribution of carrier moments for different carrier densities (for $U = 12$ and $x = 0.25$). (a) The distribution of carrier moments $P_q(M)$ for $U = 12$ case (using only $U = 12$ sites). $P_q(M)$ gets narrower up to $n = 0.3$ and broadens thereafter. This shows that moments at $n = 0.3$ are more uniform than other densities. (b) The peak of the distribution [defined as $P_q(M^*)$] for different n shows that it is optimum for $n = 0.3$.

of $n = 0.3$. We plot the peak value of moment distribution curves $P_q(M^*)$ versus n for $T = 0.01$ and 0.07 in Fig. 5(b). Next we will show that the optimization of $P_q(M^*)$ is very similar to the optimized FM, conductivity, and participation ratio (PR) windows (see Fig. 6). This emphasizes the fact that the optimum FM T_C is obtained for which the moment fluctuation at $U = 12$ sites is minimal.

Now we analyze the quantum FM structure factor for different carrier densities n at $T = 0.01$ using interacting $U = 12$ sites as mentioned in Figs. 3(a) and 5(a). For $T = 0.01$, the quantum FM structure factor as shown in Fig. 6(a) increases
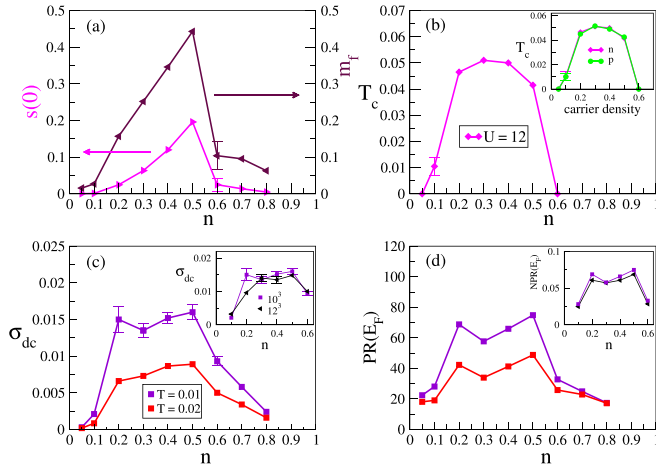

FIG. 6. Magnetic and transport properties ($U = 12$ and $x = 0.25$). (a) Quantum ferromagnetic structure factor $s(0)$ obtained for $T = 0.01$ plotted against electron densities. Uniform magnetization m_f versus electron density at $T = 0.01$ show one-to-one correspondence with $s(0)$ as it is proportional to the square root of $s(0)$. (b) Ferromagnetic window with respect to the electron density (n). The ferromagnetic transition temperature (T_C) shows optimization behavior. The inset shows the FM window for both electron and hole densities. (c) dc conductivity calculated at $T = 0.01$ shows metallicity at middle of the ferromagnetic window and depicts an insulator-metal-insulator (IMI) transition with respect to n. (d) Participation ratio around Fermi energy $PR(E_F)$ shows that the states at the middle of ferromagnetic windows are more extended and agrees well with conductivity results. Corresponding quantities for two system sizes are compared in the inset of (c) and (d).

with carrier density as expected due to the enhancement of the moments at the interacting sites [see Fig. 5(a)] and decreases sharply beyond $n = 0.5$. We also calculated the system-averaged uniform magnetization $m_f = \langle (n_\uparrow - n_\downarrow) \rangle$ for $U = 12$ sites and show that m_f goes as the square root of $s(0)$ [see Fig. 6(a)]. The nonmonotonic behavior of $s(0)$ (and m_f) around $n = 0.5$ indicates that the FM order vanishes for $n = 0.6$. The FM T_C calculated for different n, shown in Fig. 6(b), corroborates this fact. The FM window exhibits optimum ordering at the middle of the window. This emphasizes the fact that, within our s-MC calculations, a minimum amount of carrier is essential to gain considerable kinetic energy to spin polarize the system. On the other hand, for higher carrier densities, the magnetism is suppressed due to a decrease in carrier mobility as the availability of spatial interacting lattice sites decreases, which constrains the carrier movement. In the inset of Fig. 6(b), we show that the FM window and T_C remains the same for both hole and electron density calculations. The spin stiffness in spin-wave calculations in the diluted Hubbard model also poses a similar nonmonotonic picture with carrier density [54]. Similar results for magnetic impurities were also obtained in other spin-wave and MC calculations [63,89–92].

The nonmonotonic FM window signifies that the kinetic energy is minimum at the edge of the FM window. As a result, one expects a metallic system at the center of the band and an insulating state at the edge for low temperatures. In fact, conductivity calculations for different n plotted at $T = 0.01$ [see Fig. 6(c)] shows the same and depicts an insulator-metal-insulator (IMI) transition with carrier density. This also establishes the fact that the mobility is minimum near the edge of the FM window. The PR, which is a measure of the localization, is also calculated to corroborate this fact. The participation ratio PR [$= 1/\sum_i (\psi_l^i)^4$, where ψ_l^i is the normalized quasiparticle wave function for the ith site with the lth eigenvalue] provides a measure to see if the state is localized or extended. PR(E_F), which is the PR value around the Fermi energy, is shown in Fig. 6(d). Higher PR(E_F) values for ($n = 0.2 - 0.5$) shows that the states in the middle of the FM window are more extended, which agrees well with the FM T_C and conductivity data. In inset of Figs. 6(c) and 6(d), we show that the conductivity and normalized PR remains more or less the same for the two system sizes ($L = 10$ and 12).

V. COMPARISON OF FERROMAGNETIC WINDOWS FOR DIFFERENT U

Next, we explore the FM window for four different U values. The FM window in Fig. 7(a) shifts to the right with increasing U. This is because the carriers are more localized for larger U values [see in inset of Fig. 7(b)] and enhances the carrier mobility among the interacting sites due to the availability of more interacting lattice sites beyond $n = 0.5$. This analysis is true for higher density edges of the IB. In fact, in the large U ($\gg BW$) limit, the FM window is expected to span up to $n = 1.0$ like the undiluted Kondo lattice model [93,94]. At the same time, ferromagnetism in the lower part of the FM window gets depleted for stronger localization of carriers that remain localized far apart on impurity sites. The quantum FM
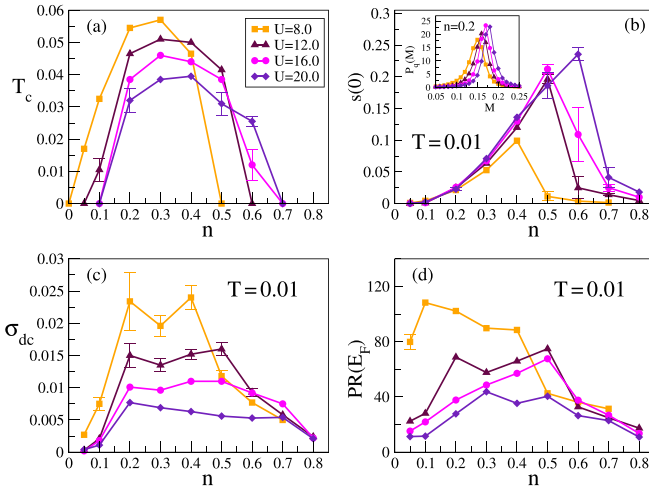
FIG. 7. Ferromagnetic windows for different U. (a) Ferromagnetic window shifts to right with U. (b) Ferromagnetic structure factor $s(0)$ versus n at $T = 0.01$. $s(0)$ for all U values show nonmonotonic behavior that agrees with the FM window. (c) dc conductivity with respect to n shows IMI pattern for different U values. (d) Participation ratio $PR(E_F)$ which is a measure of delocalization also signifies that the states corresponding to FM order are extended, though for higher U values $PR(E_F)$ decreases. Inset in (b) shows the peak of local moment distribution shift towards the carrier density value (for $n = 0.2$) for higher U and indicates the electrons are more and more localized for larger U.
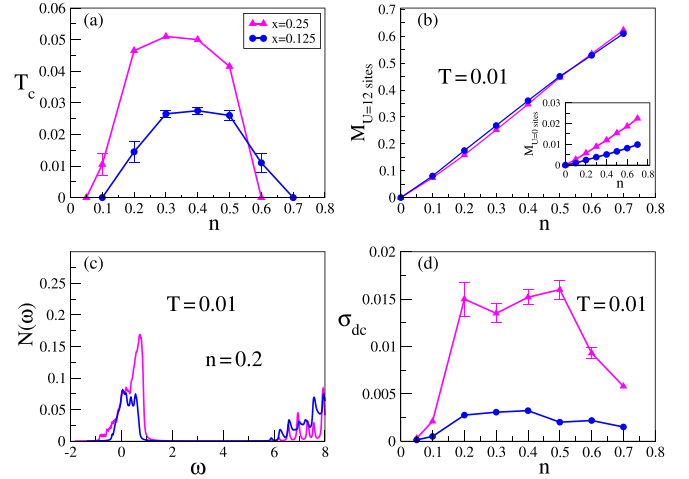

FIG. 8. Comparison of magnetic and transport properties between $x = 0.25$ and $x = 0.125$ (using $U = 12$). (a) FM window shift slightly and optimum T_c decreases considerably for $x = 0.125$. (b) Average carrier moments at $U = 12$ sites for both concentrations at different densities. Inset shows the average moments at $U = 0$ sites. (c) Density of states shows that impurity band gets narrower for smaller impurity concentration. This signify that the carriers are more localized for $x = 0.125$ as compared to $x = 0.25$. (d) dc conductivity vs n shows that the conductivity decreases for $x = 0.125$.

structure factor for different U values [see Fig. 7(b)] at low temperature ($T = 0.01$) also shows nonmonotonic behavior, similar to the $U = 12$ case. Here, for all U, the maximum $s(0)$ is found for the particular carrier density beyond which the ground state is paramagnetic. In Fig. 7(c), the conductivity results show that the IMI pattern also remains intact for all U. With increasing U, the conductivity decreases, mainly at the middle of the FM window, as carriers are more localized at larger U values. In addition, $PR(E_F)$ in Fig. 7(d) supports the localization-delocalization-localization pattern with the electron density, which is also obtained from the FM and conductivity calculations.

VI. COMPARISON OF FERROMAGNETIC WINDOWS BETWEEN $x = 0.25$ AND $x = 0.125$

In addition to $x = 0.25$, we performed systematic calculations to unveil the FM window for $x = 0.125$ case. In Fig. 8(a), we compare the FM windows for $x = 0.25$ and 0.125 using $U = 12$. Here the FM window with respect to n shifts to the right, but T_C reduces considerably. The average local moments on $U = 12$ sites remain same for both x [see Fig. 8(b)]. This indicates that the induced moment at $U = 0$ sites would decrease for smaller x. In fact, as we decrease the x the resulting moments at $U = 0$ sites decrease [see the inset of Fig. 8(b)]. Although moments for $U = 12$ sites are the same, the DOS in Fig. 8(c) shows that the carriers are more localized as the IB gets narrower for $x = 0.125$. This is due to the

increase of the distance between interacting sites in $x = 0.125$ as compared to $x = 0.25$. This is one of the reasons for the drop in T_C value. In Fig. 8(d), the reduction of conductivity with x agrees with the fact that the mobility of carriers decline for $x = 0.125$.

VII. CONCLUSIONS

In summary, based on a spin-fermion model, we show that the ferromagnetism is favored for low density of carriers, which is concomitant to the experimental results. In a nonperturbative limit ($U \sim BW$), our analysis shows that the density of the itinerant carriers, confined to the IB, that decides the kinetic energy of the system, plays an important role in determining the carrier-spin polarization. The FM ordering temperature shows an optimization behavior with the carrier density. We have provided a systematic study of carrier-spin-dependent transport properties of the carriers over the whole carrier density range. An IMI transition is observed across the FM window. Due to strong coupling between itinerant carriers and auxiliary fields, the polarization of auxiliary fields follows the property of carrier-spin polarization very closely. Thus, our results are significant for the understanding of ferromagnetism in diluted magnetic semiconductors.

[1] K. H. J. Buschow and F. R. de Boer, *Physics of Magnetism and Magnetic Materials* (Kluwer Academic/Plenum Publishers, New York, 2003).

[2] M. N. Baibich, J. M. Broto, A. Fert, F. Nguyen, Van Dau, F. Petroff, P. Etienne, G. Creuzet, A. Friederich, and J. Chazelas, Phys. Rev. Lett. **61**, 2472 (1988).

[3] G. Binasch, P. Gruenberg, F. Saurenbach, and W. Zinn, Phys. Rev. B **39**, 4828(R) (1989).

[4] H. Ohno, Nat. Mater. **9**, 952 (2010).

[5] N. A. Spaldin, *Magnetic Materials: Fundamentals and Applications* (Cambridge University Press, Cambridge, 2010).

[6] R. E. Prange and V. Korenman, Phys. Rev. B **19**, 4691 (1979).

[7] S. Sakai, R. Arita, and H. Aoki, Phys. Rev. Lett. **99**, 216402 (2007).

[8] P. Massignan, Z. Yu, and G. M. Bruun, Phys. Rev. Lett. **110**, 230401 (2013).

[9] M. Holzmann and S. Moroni, Phys. Rev. Lett. **124**, 206404 (2020)

[10] G. B. Jo, Y. R. Lee, J. H. Choi, C. A. Christensen, T. H. Kim, J. H. Thywissen, D. E. Pritchard, and W. Ketterle, Science **325**, 1521 (2009).

[11] E. C. Stoner, Proc. Roy. Soc. A **165**, 372 (1938).

[12] V. Korenman, J. L. Murray, and R. E. Prange, Phys. Rev. B **16**, 4032 (1977).

[13] M. Uhlarz, C. Pfleiderer, and S. M. Hayden, Phys. Rev. Lett. **93**, 256404 (2004).

[14] J. M. D. Coey, M. Viret, and S. V. Molnar, Adv. Phys. **48**, 167 (1999).

[15] D. Phelan, D. Louca, K. Kamazawa, M. F. Hundley, and K. Yamada, Phys. Rev. B **76**, 104111 (2007).

[16] D. J. Singh, J. Appl. Phys. **79**, 4818 (1996).

[17] W. J. Heisenberg, Z. Phys. **49**, 619 (1928).

[18] B. T. Matthias, R. M. Bozorth, and J. H. Van Vleck, Phys. Rev. Lett. **7**, 160 (1961).

[19] A. Mauger and C. Godart, Phys. Rep. **141**, 51 (1986).

[20] P. W. Anderson, Phys. Rev. **115**, 2 (1959).

[21] P. W. Anderson, *Theory of Magnetic Exchange Interactions: Exchange in Insulators and semiconductors* (Academic Press, New York, 1963).

[22] D. C. Mattis, *The Theory of Magnetism Made Simple* (World Scientific, Singapore, 2006).

[23] Z. Huang, D. Liu, Mansikkamaki, V. Vieru, N. Iwahara, and L. F. Chibotaru, Phys. Rev. Res. **2**, 033430 (2020).

[24] L. Bergqvist, Phys. Rev. Lett. **93**, 137202 (2004).

[25] S. Hilbert and W. Nolting, Phys. Rev. B **71**, 113204 (2005).

[26] V. Barzykin, Phys. Rev. B **71**, 155203 (2005).

[27] H. Munekata, H. Ohno, S. von Molnar, A. Segmüller, L. L. Chang, and L. Esaki, Phys. Rev. Lett. **63**, 1849 (1989).

[28] H. Ohno, A. Shen, F. Matsukura, A. Oiwa, A. Endo, S. Katsumoto, and Y. Iye, Appl. Phys. Lett. **69**, 363 (1996).

[29] H. Ohno, Science **281**, 951 (1998).

[30] T. Dietl, Nat. Mater. **9**, 965 (2010).

[31] T. Dietl and H. Ohno, Rev. Mod. Phys. **86**, 187 (2014).

[32] T. Jungwirth, J. Sinova, J. Masek, J. Kucera, and A. H. MacDonald, Rev. Mod. Phys. **78**, 809 (2006).

[33] C. Zener, Phys. Rev. **81**, 440 (1951).

[34] C. Zener, Phys. Rev. **83**, 299 (1951).

[35] T. Dietl, H. Ohno, F. Matsukura, J. Cibert, and D. Ferrand, Science **287**, 1019 (2000).

[36] J. Calderon and S. Das Sarma, Ann. Phys. **322**, 2618 (2007).

[37] A. H. MacDonald, P. Schiffer, and N. Samarth, Nat. Mater. **4**, 195 (2005).

[38] S. Sanvito, Pablo Ordejon, and Nicola A. Hill, Phys. Rev. B **63**, 165206 (2001).

[39] P. Mahadevan and A. Zunger, Appl. Phys. Lett. **85**, 2860 (2004).

[40] N. Samarth, Nat. Mater. **11**, 360 (2012).

[41] K. Hirakawa, S. Katsumoto, T. Hayashi, Y. Hashimoto, and Y. Iye, Phys. Rev. B **65**, 193312 (2002).

[42] V. F. Sapega, M. Moreno, M. Ramsteiner, L. Däweritz, and K. Ploog, Phys. Rev. Lett. **94**, 137401 (2005).

[43] M. Dobrowolska, K. Tivakornsasithorn, X. Liu, J. K. Furdyna, M. Berciu, K. M. Yu, and W. Walukiewicz, Nat. Mater. **11**, 444 (2012).

[44] L. Kronik, M. Jain, and J. R. Chelikowsky, Phys. Rev. B **66**, 041203(R) (2002).

[45] R. Y. Korotkov, J. M. Gregie, and B. W. Wessels, Appl. Phys. Lett. **80**, 1731 (2002).

[46] R. Bouzerar and G. Bouzerar, Europhys. Lett. **92**, 47006 (2010).

[47] T. Jungwirth, J. Sinova, A. H. MacDonald, B. L. Gallagher, V. Novak, K. W. Edmonds, A. W. Rushforth, R. P. Campion, C. T. Foxon, L. Eaves, E. Olejnik, J. Masek, S. R. Eric Yang, J. Wunderlich, C. Gould, L. W. Molenkamp, T. Dietl, and H. Ohno, Phys. Rev. B **76**, 125206 (2007).

[48] S. Ohya, K. Takata, and M. Tanaka, Nat. Phys. **7**, 342 (2011).

[49] K. Ando, H. Saito, K. C. Agarwal, M. C. Debnath, and V. Zayets, Phys. Rev. Lett. **100**, 067204 (2008).

[50] K. S. Burch, D. B. Shrekenhamer, E. J. Singley, J. Stephens, B. L. Sheu, R. K. Kawakami, P. Schiffer, N. Samarth, D. D. Awschalom, and D. N. Basov, Phys. Rev. Lett. **97**, 087208 (2006).

[51] K. Sato, L. Bergqvist, J. Kudrnovsky, P. H. Dederichs, O. Eriksson, I. Turek, B. Sanyal, G. Bouzerar, H. Katayama-Yoshida, V. A. Dinh, T. Fukushima, H. Kizaki, and R. Zeller, Rev. Mod. Phys. **82**, 1633 (2010).

[52] R. C. Myers, B. L. Sheu, A. W. Jackson, A. C. Gossard, P. Schiffer, N. Samarth, and D. D. Awschalom, Phys. Rev. B **74**, 155203 (2006).

[53] K. M. Yu, W. Walukiewicz, T. Wojtowicz, I. Kuryliszyn, X. Liu, Y. Sasaki, and J. K. Furdyna, Phys. Rev. B **65**, 201303(R) (2002).

[54] A. Singh, Animesh Datta, S. K. Das, and V. A. Singh, Phys. Rev. B **68**, 235208 (2003).

[55] A. Mukherjee, N. D. Patel, S. Dong, S. Johnston, A. Moreo, and E. Dagotto, Phys. Rev. B **90**, 205133 (2014).

[56] S. Chakraborty, A. mukherjee, and K. Pradhan, Phys. Rev. B **106**, 075146 (2022).

[57] M. Ulmke, P. J. H. Denteneer, R. T. Scalettar, and G. T. Zimanyi, Europhys. Lett. **42**, 655 (1998).

[58] M. Qin, H. Shi, and S. Zhang, Phys. Rev. B **96**, 075156 (2017).

[59] H. Shi and S. Zhang, Phys. Rev. B **88**, 125132 (2013).

[60] K. Bouadim, N. Paris, F. Hebert, G. G. Batrouni and R. T. Scalettar, Phys. Rev. B **76**, 085112 (2007).

[61] J. E. Hirsch, Phys. Rev. B **31**, 4403 (1985).

[62] S. Kumar and P. Majumdar, Eur. Phys. J. B **50**, 571 (2006).

[63] S. Chakraborty, S. K. Das, and K. Pradhan, Phys. Rev. B **102**, 245112 (2020).

[64] M. Ulmke, Eur. Phys. J. B **1**, 301 (1998).

[65] T. Obermeier, T. Pruschke, and J. Keller, Phys. Rev. B **56**, R8479(R) (1997).

[66] M. Kollar and D. Vollhardt, Phys. Rev. B **63**, 045107 (2001).

[67] K. Edmonds, S. V. Novikov, M. Sawicki, R. P. Campion, C. R. Staddon, A. D. Giddings, L. X. Zhao, K. Y. Wang, T. Dietl, C. T. Foxon, and B. L. Gallagher, Appl. Phys. Lett. **86**, 152114 (2005).

[68] J. M. D. Coey, M. Venkatesan, and C. B. Fitzgerald, Nat. Mater. **4**, 173 (2005).

[69] Q. Xu, L. Hartmann, S. Zhou, A. Mcklich, M. Helm, G. Biehne, H. Hochmuth, M. Lorenz, M. Grundmann, and H. Schmidt, Phys. Rev. Lett. **101**, 076601 (2008).

[70] E. Dagotto, *Nanoscale Phase Separation and Colossal Magnetoresistance: The Physics of Manganites and Related Compounds* (Springer, Berlin, 2003).

[71] G. D. Mahan, *Quantum Many Particle Physics* (Plenum Press, New York, 1990).

[72] S. Kumar and P. Majumdar, Europhys. Lett. **65**, 75 (2004).

[73] P. Bulanchuk, Comput. Phys. Commun. **261**, 107714 (2021).

[74] S. Kumar and P. Majumdar, Eur. Phys. J. B **46**, 237 (2005).

[75] R. A. de Groot, F. M. Mueller, P. G. van Engen, and K. H. J. Buschow, Phys. Rev. Lett. **50**, 2024 (1983).

[76] K. E. H. M. Hanssen, P. E. Mijnarends, L. P. L. M. Rabou, and K. H. J. Buschow, Phys. Rev. B **42**, 1533 (1990).

[77] M. I. Katsnelson, V. Yu. Irkhin, L. Chioncel, A. I. Lichtenstein, R. A. de Groot, Rev. Mod. Phys. **80**, 315 (2008).

[78] M. Jourdan, J. Minar, J. Braun, A. Kronenberg, S. Chadov, B. Balke, A. Gloskovskii, M. Kolbe, H. J. Elmers, G. Scoenhense, H. Ebert, C. Felser, and M. Klaeu, Nat. Commun. **5**, 3974 (2014).

[79] R. Shan, H. Sukegawa, W. H. Wang, M. Kodzuka, T. Furubayashi, T. Ohkubo, S. Mitani, K. Inomata, and K. Hono, Phys. Rev. Lett. **102**, 246601 (2009).

[80] K. Schwarz, J. Phys. F: Met. Phys. **16**, L211 (1986).

[81] J. H. Park, E. Vescovo, H. J. Kim, C. Kwon, R. Ramesh, and T. Venkatesan, Nature (London) **392**, 794 (1998).

[82] Y. S. Dedkov, U. Ruediger, and G. Guentherodt, Phys. Rev. B **65**, 064417 (2002).

[83] K. P. Kaemper, W. Schmitt, G. uentherodt, R. J. Gambino, and R. Ruf, Phys. Rev. Lett. **59**, 2788 (1987).

[84] P. A. Dowben and R. Skomski, J. App. Phys. **95**, 7453 (2004).

[85] B. Nadgorny, J. Phys.: Condens. Matter **19**, 315209 (2007).

[86] J. G. Tobin, S. A. Morton, S. W. Yu, G. D. Waddill, I. K. Schuller, and S. A. Chambers, J. Phys.: Condens. Matter **19**, 315218 (2007).

[87] N. A. Spaldin, Phys. Rev. B **69**, 125201 (2004).

[88] L. H. Ye, A. J. Freeman, and B. Delley, Phys. Rev. B **73**, 033203 (2006).

[89] G. Alvarez, M. Mayr, and E. Dagotto, Phys. Rev. Lett. **89**, 277202 (2002).

[90] A. Singh, S. K. Das, A. Sharma, and W. Nolting, J. Phys.: Condens. Matter **19**, 236213 (2007).

[91] K. Pradhan and S. K. Das, Sci. Rep. **7**, 9603 (2017).

[92] D. H. Bui, Q. H. Ninh, and H. N. Nguyen, and V. N. Phan, Phys. Rev. B **99**, 045123 (2019).

[93] S. Yunoki, J. Hu, A. L. Malvezzi, A. Moreo, N. Furukawa, and E. Dagotto, Phys. Rev. Lett. **80**, 845 (1998).

[94] K. Pradhan and P. Majumdar, Europhys. Lett. **85**, 37007 (2009).